

A broadband wavelet implementation for rapid ultrasound pulse-echo time-of-flight measurements

Cite as: Rev. Sci. Instrum. 91, 075115 (2020); doi: 10.1063/5.0010475

Submitted: 10 April 2020 • Accepted: 6 July 2020 •

Published Online: 22 July 2020



Blake T. Sturtevant,^{1,2,a)} Nenad Velisavljevic,^{2,b)} Dipen N. Sinha,¹ Yoshio Kono,^{3,c)} and Cristian Pantea¹

AFFILIATIONS

¹Materials Physics and Applications Division, Los Alamos National Laboratory, Los Alamos, New Mexico 87545, USA

²Explosive Science and Shock Physics Division, Los Alamos National Laboratory, Los Alamos, New Mexico 87545, USA

³HPCAT, Geophysical Laboratory, Carnegie Institution of Washington, Argonne, Illinois 60439, USA

^{a)}Author to whom correspondence should be addressed: bsturtev@lanl.gov

^{b)}Currently at: Physics Division, Physical and Life Sciences Directorate, Lawrence Livermore National Laboratory, Livermore, CA 94550, USA.

^{c)}Currently at: Geodynamics Research Center, Ehime University, Matsuyama, Ehime 790-8577, Japan.

ABSTRACT

A broadband wavelet approach to ultrasonic pulse-echo time-of-flight measurements is described. The broadband approach significantly reduces the time required for frequency-dependent pulse-echo measurements, enabling studies of dynamic systems ranging from biological systems to solid-state phase transitions. The described broadband approach is demonstrated in parallel with the more traditional frequency stepping approach to perform ultrasound time-of-flight measurements inside a large volume Paris-Edinburgh press *in situ* at a synchrotron source. The broadband wavelet data acquisition process was found to be 1–2 orders of magnitude faster than the stepped-frequency approach, with no compromise on data quality or determined results.

© 2020 Author(s). All article content, except where otherwise noted, is licensed under a Creative Commons Attribution (CC BY) license (<http://creativecommons.org/licenses/by/4.0/>). <https://doi.org/10.1063/5.0010475>

I. INTRODUCTION

There are many practical applications where accurate and fast, even time-resolved, sound speed measurements are highly desirable. For example, ultrasonic studies of pressure-induced solid–melt and solid–solid phase transitions can provide valuable insight into the mechanisms and kinetics of processes with characteristic times of the order of milliseconds to seconds.¹ Additionally, biological processes (e.g., heart beating, breathing, and muscle flexion and relaxation) often occur over time scales of the order of one second. Pulsed fields at the National High Magnetic Field Laboratory range in duration from 25 ms to 2.5 s,² so sound speed data acquisition must be significantly faster than this to resolve changes in the sound speed within a changing magnetic field. A final example, and the one that will be highlighted here, is the measurement of sound speeds

inside a large volume pressure cell *in situ* at a synchrotron facility. In this application, streamlining and accelerating data acquisition is important for optimizing the use of limited and valuable beam time. Additionally, stabilizing the pressure in the high pressure system for extended periods can be challenging due to the relaxation of the sample and pressure cell components.

Ultrasonic pulse-echo measurements have been used for more than 70 years as one method of accurately determining sound speeds (and, thus, elastic moduli) from a measured ultrasonic wave time-of-flight.^{3,4} In pulse-echo measurements, the difference in arrival times of ultrasonic echoes from the opposite sides of a sample is used to determine the round trip time-of-flight of the wave in the sample, τ_s . Taken together with a measurement of the physical length of the sample (l), this yields the group velocity, v , of the ultrasonic wave: $v = 2l/\tau_s$. As fundamental thermodynamic properties,

a material's longitudinal (polarized along the direction of propagation) and shear (transversely polarized) sound speeds play an important role in constraining pressure–volume–temperature equations of state for a material.^{5,6} The longitudinal and shear ultrasonic phase velocities can also be used, along with other properties such as mass density, thermal conductivity, and temperature, to determine many important thermodynamic properties of a material. Some of these properties include the full tensor of elasticity, the Grüneisen parameter, the elastic Debye temperature, the acoustic thermal conductivity, and the isothermal bulk modulus.⁷

An important, yet frequently overlooked, consideration in ultrasonic pulse echo measurements is that the wave acquires phase shifts upon reflection from and transmission through the interface of the sample and the materials surrounding it. Taken together, these lead to a net phase shift (ϕ_{net}) between the echoes that results in a difference in the time measured (τ_m) between the two sample echoes and the actual desired time-of-flight in the sample τ_s ,

$$\tau_m(f) = \tau_s + \frac{\phi_{net}}{2\pi f}. \quad (1)$$

Attempts to correct for this phase shift both theoretically and experimentally have previously been reported.^{4,8–11} In the present work, the method in Refs. 4, 10, and 11 is adopted, where $\tau_m(f)$ are measured over a range of frequencies and the results are plotted vs $1/f$. A linear fit to $\tau_m(f)$ vs $1/f$ is performed, and the y-intercept of these data yield the desired τ_s . The magnitude of the correction achieved by using this technique compared to measuring $\tau_m(f)$ at a single frequency depends in an absolute sense on the period of the carrier signal used. However, the magnitude of the relative (%) correction depends also on the value of τ_s with shorter times-of-flight having a larger relative correction for a given ϕ_{net} . This procedure, while providing the most accurate value of τ_s , has a time intensive data acquisition process that can last for several tens of minutes, with the total time depending on the number of $\tau_m(f)$ measured as well as the number of waveforms averaged for each data point. A broadband signal approach enabling faster data acquisition has previously been reported in Ref. 12, in which a transfer function of a system (i.e., transducer, buffer rod, sample) is recorded and the impulse response is later convolved with a pure RF tone to simulate real time pulse echo measurements.

In this work, a straightforward approach is demonstrated to rapidly determine the frequency-corrected time-of-flight in a pulse echo measurement using a single broadband waveform. This single waveform is subsequently digitally signal processed to extract the same information as would be attained by sequentially stepping through a large number of frequencies. The experiments described here consist of ultrasound pulse-echo time-of-flight measurements as a function of pressure inside a Paris–Edinburgh large volume press at the HPCAT (High Pressure Collaborative Access Team) sector of the Advanced Photon Source at Argonne National Laboratory. The broadband signal employed here is a Gaussian wavelet with a user defined center frequency and full-width-half-maximum bandwidth. However, any signal with a suitably high bandwidth, such as a $\text{sinc}(x) = \sin(x)/x$, can be used to accomplish similar results.

II. EXPERIMENTAL APPROACH

The pressure dependence of a material's sound speeds (and other thermodynamic properties mentioned above) can be determined by performing ultrasonic pulse-echo time-of-flight measurements inside a large volume pressure cell, such as a Paris–Edinburgh style press, as detailed in Ref. 13. Briefly, the “inner cell” assembly, shown in an exploded view in Fig. 1(a) and in a cross-sectional view in Fig. 1(b), is compressed axially between two tungsten carbide (WC) anvils whose cupped geometry mates with the top and bottom zirconia caps of the inner cell assembly. The top WC anvil is fitted with a piezoelectric transducer that introduces an ultrasonic wave into the anvil. The transducer used here is a 10° Y-rotated lithium niobate single crystal, 2.54 mm in diameter, that generates longitudinal and shear ultrasound waves with fundamental frequencies of 50 MHz and 30 MHz, respectively. For simplicity, only the longitudinal mode will be discussed here. The wave travels through the anvil and then into the alumina (Al_2O_3) buffer rod, the sample, and the silica (SiO_2) glass backing plate, partially reflecting at each interface where there is a change in acoustic impedance.¹⁴ After reflection from each interface, the wave travels back to the transducer where its arrival is digitized using an oscilloscope. Figure 2 shows an example waveform of a longitudinally polarized ultrasound wave off of the following interfaces: (i) WC anvil-alumina buffer rod, (ii) alumina buffer rod-sample, (iii) sample-silica glass backing plate, and (iv) silica glass backing plate-alumina support plate. At interfaces (i) and (ii), a 2.5 μm thick gold foil is used as a coupling layer to maximize ultrasonic energy transmission. The sample used in the experiments described in this work was a polycrystalline tantalum cylinder with a diameter of 1.5 mm and a thickness of 535 μm .

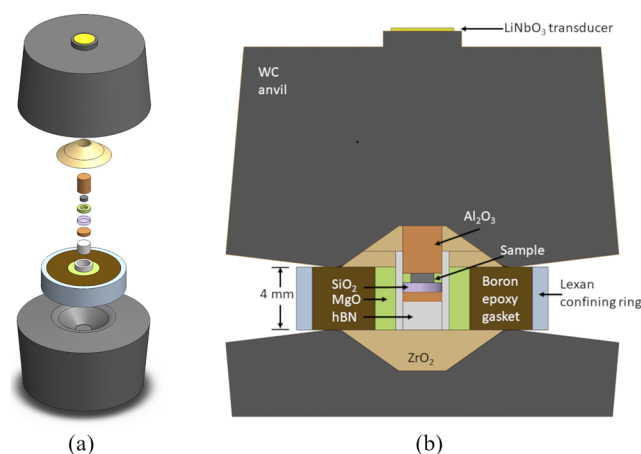


FIG. 1. The high pressure inner cell assembly, including sample, used in this work is shown in the exploding view (a) and in the cross-sectional view (b). The ultrasonic transducer (gold colored) can be seen mounted on top of the upper WC anvil (a). The cylindrical sample is surrounded by concentric rings and cylinders of silica glass (SiO_2), alumina (Al_2O_3), hexagonal boron nitride (hBN), magnesia (MgO), and zirconia (ZrO_2). The various components are chosen to simultaneously provide support to maintain the cylindrical shape of the sample, to provide a pressure marker, and to provide a quasi-hydrostatic sample environment. The boron epoxy gasket and lexan confining ring enable radial x-ray diffraction from the sample.

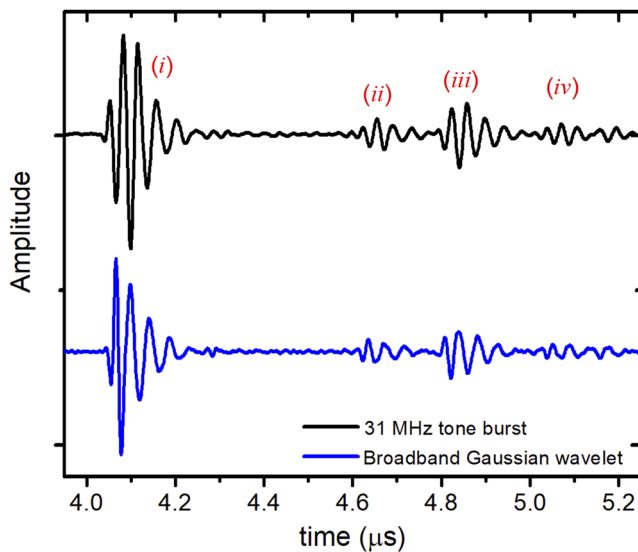


FIG. 2. Example echoes of a longitudinally polarized ultrasonic wave from the sample and other components of the inner cell assembly. The top waveform was collected using a 31 MHz tone burst, and the bottom waveform was collected using the broadband Gaussian wavelet described in the text. The first echo to arrive (i) is from the interface between the tungsten carbide anvil and the alumina buffer rod (Fig. 1). Subsequent echoes are from the buffer rod-sample interface (ii), the sample-silica glass plate interface, (iii) and the silica glass-alumina plate interface (iv). The measured time-of-flight in the sample, τ_m , is the time difference between echoes (ii) and (iii).

at laboratory ambient pressure and 350 μm at 7.1 GPa, the maximum pressure achieved in this example. The other components of the pressure cell assembly, specifically the hexagonal boron nitride (hBN) and MgO parts, are used to achieve a quasi-hydrostatic environment and to allow for sample pressure determination from x-ray diffraction from a material (MgO) with a well-known P-V-T equation of state.¹⁵ The experimental hardware (i.e., arbitrary function

generator, digitizing oscilloscope, directional bridge) in this work was the same as described in Ref. 13 with the exception of the preamplifier used in this work (Narda-MITEQ model AM-2A-000110), which was chosen to enable measurements at higher frequencies.

Data were collected at 28 pressures between 2 GPa and 7.1 GPa. At each pressure, data were collected first using the traditional approach (i.e., by sequentially sending out tone bursts of increasing carrier frequency over the frequency range of interest) and also by collecting a single broadband Gaussian wavelet. For the data collected using the traditional approach, single-frequency tone bursts 0.1 μs in duration were collected using carrier frequencies between 17 MHz and 67 MHz in 2 MHz steps for a total of 26 waveforms. A Tukey Envelope with a shaping parameter, $\alpha = 0.7$,¹⁶ was applied to the tone burst to mitigate the high frequency effects arising from the use of a rectangular window.¹⁰

III. RESULTS and DISCUSSION

The Gaussian wavelet is used here to refer to a train of pulses in the time domain that have a Gaussian shape in the frequency domain. The Gaussian wavelet used in this work is of the form

$$\Psi\left(t - \frac{x}{c}\right) = A \int df \cos\left(2\pi f\left[t - \frac{x}{c}\right]\right) e^{-(f-f_0)^2/2\sigma^2}. \quad (2)$$

Here, t , x , and c represent the time, distance propagated, and speed of the wave, respectively, and the integral is carried out over all frequencies, f . The three free parameters, f_0 , σ , and A , represent the center carrier frequency, the half-width-half-maximum of the wavelet in the frequency domain, and the signal amplitude, respectively. For practical implementation, this wavelet is integrated and simplified in Mathematica, yielding a complex expression. The real part of this expression at zero phase ($x = 0$) is, then, passed to the function generator,

$$\Re\{\Psi(t)\} = A \sqrt{\frac{\pi}{2}} \sigma e^{-2\pi^2 \sigma^2 t^2} [\cos(2\pi f_0 t) + \cos(2\pi f_0 t) \cos(4\pi f_0 t) + \sin(2\pi f_0 t) \sin(4\pi f_0 t)]. \quad (3)$$

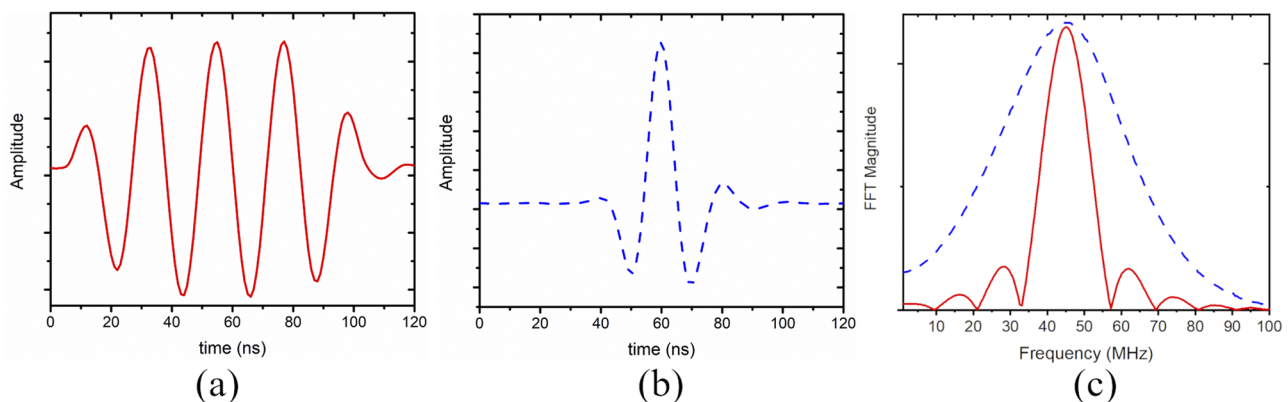


FIG. 3. Examples of a 45 MHz tone burst (a) and 45 MHz Gaussian wavelet with $\sigma = 20$ MHz (b) in the time domain. The Gaussian wavelet is significantly shorter in duration, making it easy to distinguish echoes that are close together in time (i.e., from small samples). The frequency content of the two signals are compared in (c) with the Gaussian wavelet shown by the blue (dashed) line. The Gaussian wavelet has a larger bandwidth, allowing for the frequency dependent phase correction from a single waveform.

For comparison with the traditional approach, a single Gaussian broadband wavelet with $f_0 = 45$ MHz and $\sigma = 20$ MHz was collected at each pressure. Figure 3 compares a 45 MHz tone burst as is typically used in the traditional approach (a) with the broadband Gaussian wavelet used in this study (b) in the time domain. One main advantage of using a broadband pulse in the time domain is that the signal duration is much shorter than is typically used for a tone burst [100 ns in Fig. 3(a) example], which allows for the separation of echoes from very small samples that will arrive very close to each other in time. Figure 3(c) compares the frequency content of the tone burst (solid red line) to that of the Gaussian wavelet (dashed blue line). Because of its large bandwidth, the single Gaussian pulse provides the same information as many different single

frequency tone bursts. A slight DC offset is observed in the Gaussian wavelet signal [Figs. 3(b) and 3(c)], although this has no effect on the determined time-of-flight. To determine the sound speed and other thermodynamic properties from the measured transit times, the pressure inside the pressure cell, the mass density, and the physical dimensions of the sample were measured directly by energy dispersive x-ray diffraction and x-ray radiography, respectively, as described elsewhere.¹³

The data for the traditional approach were analyzed using the method described in Refs. 10 and 11, which is visually summarized in Fig. 4 for a single frequency ($f = 31$ MHz in this example). At each frequency for which data were collected, the ultrasonic echoes from the top and bottom of the sample (echoes *ii* and *iii* in Fig. 2)

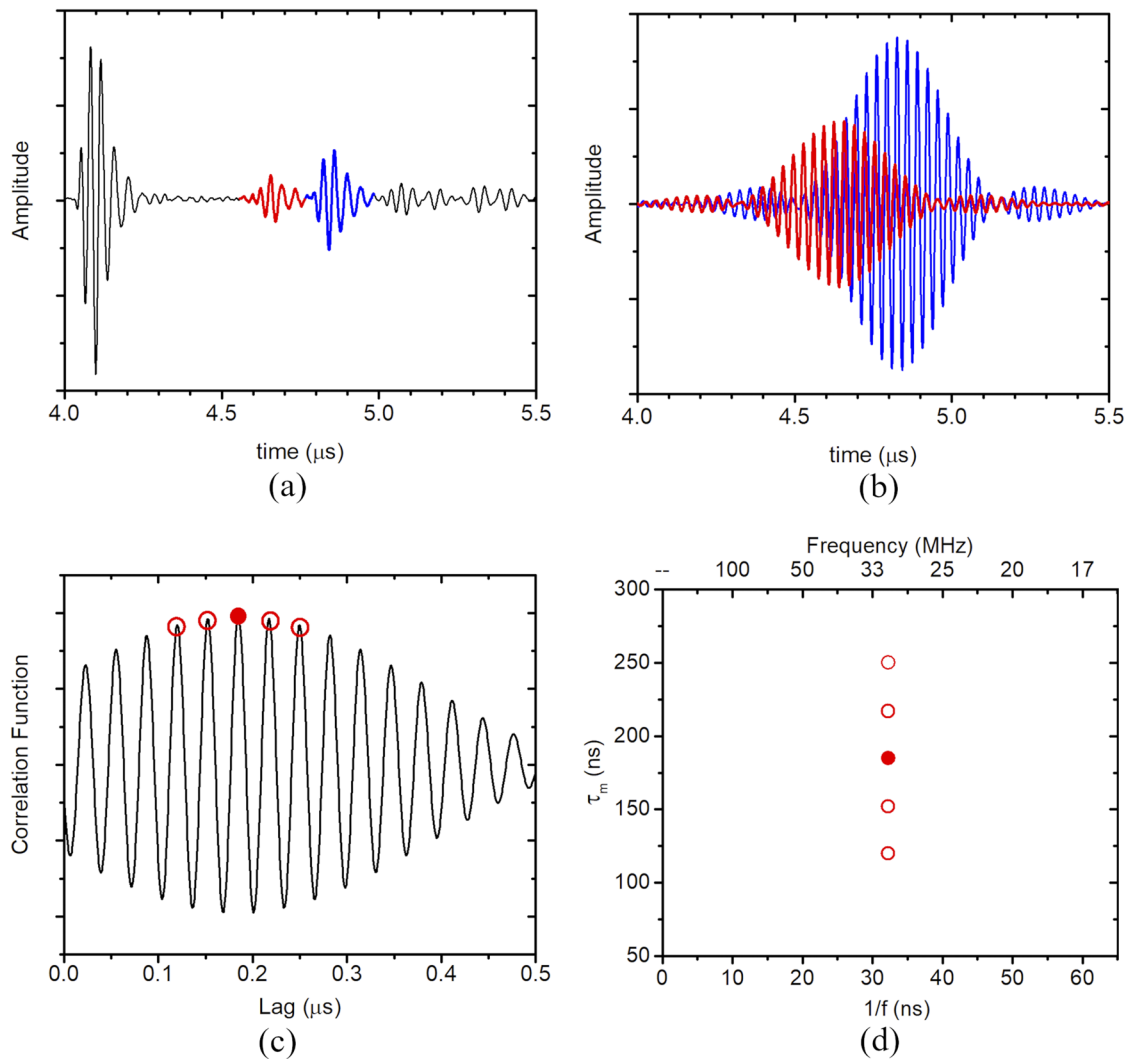


FIG. 4. The data analysis procedure for couplant corrected pulse-echo measurements, shown for a single frequency (31 MHz). (a) Echoes of interest are windowed from the raw, as-collected, waveform (black trace). Echoes (*ii*) and (*iii*) from Fig. 2 are windowed and shown with heavy red and blue traces, respectively. In (b), the windowed echoes are individually filtered using a third order Butterworth bandpass filter with a passband of $\pm 5\%$ of the carrier frequency (31 MHz in this example). (c) The windowed, filtered echoes are then cross-correlated and the maximum (solid circular marker) and two local maxima before and after the maximum are identified. Finally, in (d), the identified maxima are plotted vs $1/f$ at each frequency for which data are collected (only 31 MHz shown here).

were windowed [Fig. 4(a)], digitally bandpass filtered [Fig. 4(b)], and cross-correlated [Fig. 4(c)]. In Fig. 4(a), the raw waveform is plotted in black, while the thicker red and blue sections show the windowed echoes *ii* and *iii*, respectively. The windowed echoes were then filtered using a third order Butterworth filter with a passband of $\pm 5\%$ of the carrier frequency [Fig. 4(b)]. The bandpass filter is used to provide as pure a frequency as was reasonably achievable because even a tone burst has a finite non-zero bandwidth [Fig. 3(c)]. Figure 4(c) shows the cross-correlation of the windowed, filtered echoes. The maximum in the correlation function is identified using a solid marker while several local maxima in the correlation function on each side of the global maximum are marked using open circles. As shown in Refs. 10 and 11, it is important to consider multiple maxima in the correlation function in order to properly distinguish the maximum with a net phase of ϕ_{net} from those with phases of $\phi_{net} \pm (2\pi, 4\pi, \dots)$. The delay, τ_m , at which the maximum in the cross-correlation function occurs for the tone burst with carrier frequency $f = 31$ MHz, along with two maxima at both shorter and longer phase delays, are plotted vs inverse frequency in Fig. 4(d). The procedure described above is performed separately for each of the 26 waveforms collected; Fig. 5 shows the equivalent of Fig. 4(d) with data for all frequencies plotted. In addition, shown in Fig. 5 are linear fits to the maxima in the correlation functions. Extrapolation of these fits to $f \rightarrow \infty$ allows for the determination of the vertical intercept, which provides the desired time of flight in the sample, τ_s , from Eq. (1). It should be noted that this analysis procedure is only valid for nondispersive materials. If the sample material is dispersive,

τ_s will itself be a function of frequency and the simple linear model of Eq. (1) cannot be used.

Analysis for the Gaussian wavelet proceeds in essentially the same manner as for the traditional approach described above, except that a single raw broadband waveform, containing all of the frequencies of interest, is used. The equivalent of the analysis steps depicted in Figs. 4(b)–4(d) proceeds for the Gaussian wavelet while the same single broadband [equivalent of Fig. 4(a)] is used for all frequencies of interest. Figure 6(a) shows the equivalent of Fig. 4(a) for the Gaussian wavelet, while Figs. 6(b)–6(d) show the equivalent of Fig. 4(b) for the three selected frequencies ($f = 25$ MHz, 45 MHz, and 65 MHz). These three frequencies were selected because they coincide with the lowest, center, and highest frequencies of the Gaussian wavelet used here, respectively, with the upper and lower bounds being defined by the half-maximum of the Gaussian in the frequency domain. Using the broadband Gaussian wavelet technique, equivalent datasets can be generated for as many frequencies as is desired by simply changing the center frequency of the bandpass filter. In contrast, generating data at additional or finely spaced frequencies using the traditional approach comes at the, potentially significant, cost of time in the data acquisition process. For a direct comparison in this work, the Gaussian wavelet echoes were windowed and filtered at the same frequencies as used in the traditional approach. After windowing and filtering, the echoes were cross-correlated to determine the measured time-of-flight τ_m . These analyses were performed, and the τ_s determined, for each of the 28 pressures at which data were collected.

Figure 5 compares the determined τ_m for the data collected using the traditional approach (open circles) to those collected at a pressure of 4.3 GPa using the single Gaussian wavelet (cross-markers). Linear fits to the data plotted vs $1/f$ (only the fits to the traditional approach are shown in Fig. 4, for clarity) extrapolated to $1/f = 0$ yield $\tau_s = 176.0$ ns and 176.3 ns for the traditional approach and Gaussian wavelet, respectively. The uncertainty in the τ_s values, estimated from the linear fit statistics, is ~ 0.5 ns for both the broadband and traditional approaches. It can be noted from the figure that the two approaches agree remarkably well at high frequency and only slightly start to diverge at lower frequencies (< 25 MHz). The low frequency discrepancy can be attributed to the order of data collection. The pressure in the hydraulic press, and, thus, the pressure at the sample, changed slightly during the course of data acquisition for the traditional approach. Figure 7 compares the determined τ_s using the two approaches at each pressure at which data were collected. The agreement between the two approaches is very good, with a mean absolute difference in the τ_s of 0.7 ns in good agreement with the 0.5 ns uncertainty in τ_s . The abrupt changes in τ_s at pressures of ~ 3.5 GPa and 5 GPa may result from the yielding of various components of the cell assembly (Fig. 1) under different loads. It was observed that the sample dimensions, measured by *in situ* x-ray radiography, also show abrupt changes at the same pressures. When the time-of-flight measurements are combined with the sample length measurements, sound speeds and elastic moduli change smoothly and monotonically as a function of pressure.

The time required for data acquisition depends on multiple factors, such as the trigger interval of the function generator, the number of averages needed to achieve an acceptable signal to noise ratio and, in the case of the traditional approach, the number of

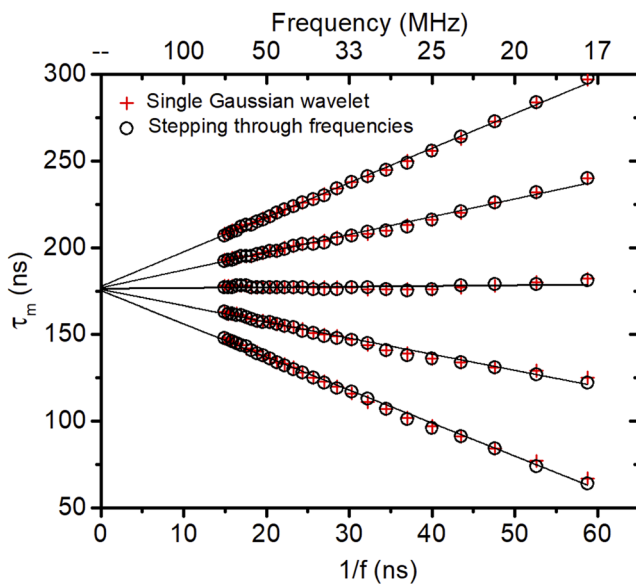


FIG. 5. The measured time-of-flight τ_m , are plotted vs $1/f$ to determine the time-of-flight in the sample, t_s , as described in the text. In addition, shown are the linear fits used to determine the intercept value, τ_s . Data points determined using a single broadband Gaussian wavelet (cross-markers) are seen to be in excellent agreement with those collected using the traditional approach (open circles) consisting of 26 separate measurements. The two datasets above and below the shallowest line have slopes of $\phi_{net} \pm 2\pi$ and $\phi_{net} \pm 4\pi$ and are retained for reasons described elsewhere.^{10,11}

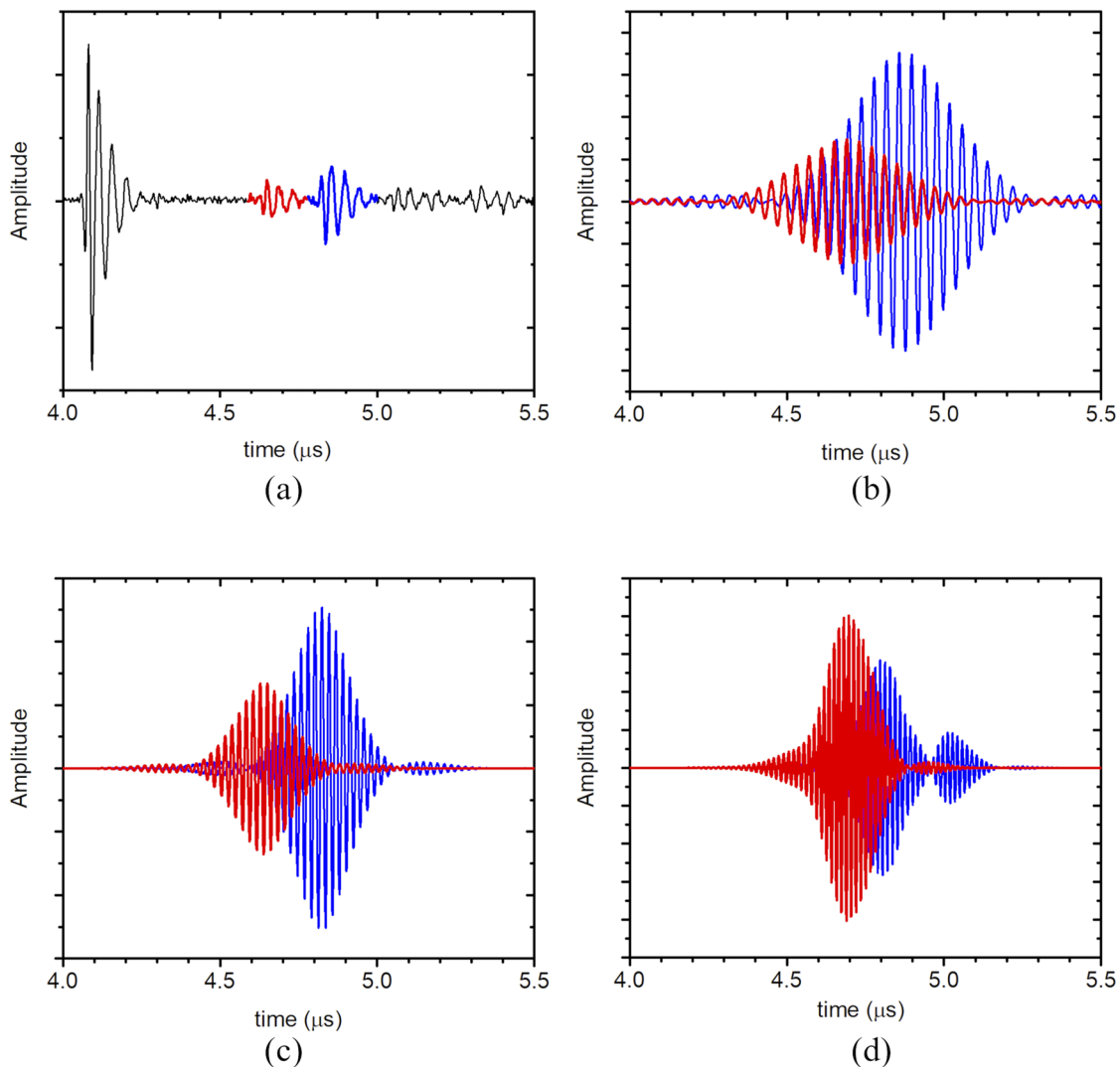


FIG. 6. Generating datasets at many frequencies using a single broadband Gaussian wavelet. (a) The raw waveform (black) as well as windowed echoes of interest [red and blue correspond to echoes (ii) and (iii) in Fig. 2, respectively] collected using a single broadband Gaussian wavelet. By filtering the windowed echoes from this single waveform, filtered echoes equivalent to those shown in Fig. 4(b) can be generated over a wide range of frequencies. (b)–(d) show the effect of passing the windowed echoes through a bandpass filter with center frequencies of 25 MHz, 45 MHz, and 65 MHz, respectively.

frequencies that are stepped through. For a given system (i.e., transducer, buffer rod, couplant, and sample at a potentially extreme temperature, pressure, or field condition), the number of averages required to achieve sufficient signal to noise is essentially the same for both the broadband Gaussian wavelet and a single frequency tone burst. Therefore, the time savings of the broadband Gaussian wavelet technique with respect to the traditional approach depends entirely on how many frequencies would be sampled in the traditional approach. Before digitizing oscilloscopes were available, it was common to perform measurements at only two frequencies to account for the couplant layer.⁴ More recent work, which used very closely spaced frequency steps to investigate the suitability of

a non-linear model for the couplant correction, used 1800 frequencies between 35 MHz and 125 MHz.¹¹ The potential data acquisition time saved by using the broadband approach in these two examples, thus, ranges from between 2 and nearly 2000 times with respect to the traditional approach. In typical applications, the number of frequencies sampled is of the order 10 or 100, as in Fig. 5, where 26 frequencies were used. With respect to time-resolved measurements, ultra-fast experiments such as those involving pulsed fields or material phase transitions may necessitate the collection of waveforms, which are either single shot or involve very few waveform averages. For example, in the case of the 25 ms pulsed fields mentioned in the Introduction, 50 single shot waveforms could be collected

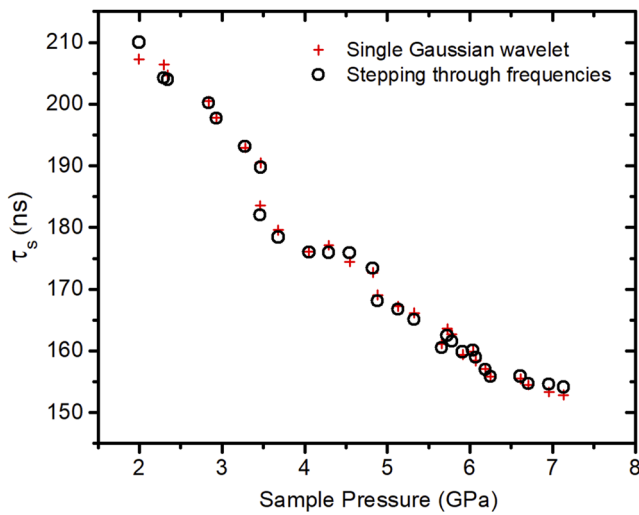


FIG. 7. Determined sample time-of-flights, τ_s , for a longitudinally polarized ultrasonic wave as a function of pressure up to 7.1 GPa. The values determined from the single Gaussian wavelet and the traditional approach are within their respective uncertainties. Together with the sample dimensions determined using radiography, these values are used to determine the speed of sound and the compressional elastic modulus.

during the pulse using a 0.5 ms trigger interval. Even if 10 waveforms are needed to be averaged for each data point, the collection of five data points would be still be enough.

IV. CONCLUSION

A rapid broadband implementation of the ultrasonic pulse-echo technique for determining accurate couplant-corrected sound speeds has been described in this work. The power of the technique lies in the use of a broadband Gaussian ultrasonic signal, which enables a frequency-dependent correction to ultrasonic time-of-flight data with as much information in a single waveform as provided by many (26 in this study) independently collected tone burst waveforms. The broadband technique enables data acquisition that is 1–2 orders of magnitude faster than the traditional approach in most typical applications, as seen in the factor of 26 time savings in the example highlighted above. In this work, the broadband approach has been demonstrated using the example of high pressure ultrasound measurements *in situ* at a synchrotron beamline. The approach is readily extensible to a host of other dynamic applications in applied science where data acquisition time is an important consideration, such as material phase transitions, ultrasound measurements in pulsed fields, and many biological processes.

ACKNOWLEDGMENTS

The authors thank Mr. Eric Moss for help in developing the data acquisition software and for assistance with data collection. Los Alamos National Laboratory (LANL) is operated by Triad National Security, LLC for the DOE-NNSA under Contract

No. 89233218CNA000001. The authors acknowledge funding support from LANL Science Campaign 2. Portions of this work were performed at HPCAT (Sector 16), Advanced Photon Source (APS), Argonne National Laboratory. HPCAT operations are supported by DOE-NNSA's Office of Experimental Sciences. The Advanced Photon Source is a U.S. Department of Energy (DOE) Office of Science User Facility operated for the DOE Office of Science by Argonne National Laboratory under Contract No. DE-AC02-06CH11357. Y.K. acknowledges the support from DOE-BES/DMSE under Award No. DE-FG02-99ER45775.

DATA AVAILABILITY

The data that support the findings of this study are available from the corresponding author upon reasonable request.

REFERENCES

- N. V. C. Shekar and K. G. Rajan, "Kinetics of pressure induced structural phase transitions—A review," *Bull. Mater. Sci.* **24**, 1–21 (2001).
- Los Alamos National Laboratory, National High Magnetic Field Laboratory—Magnets, April 10, 2020, available at: <https://nationalmaglab.org/user-facilities/pulsed-field-facility/instruments-pff/>.
- H. B. Huntington, "Ultrasonic measurements on single crystals," *Phys. Rev.* **72**, 321–331 (1947).
- H. J. Mcskimin, "Pulse superposition method for measuring ultrasonic wave velocities in solids," *J. Acoust. Soc. Am.* **33**, 12–16 (1961).
- E. H. Abramson and J. M. Brown, "Equation of state of water based on speeds of sound measured in the diamond-anvil cell," *Geochim. Cosmochim. Acta* **68**, 1827–1835 (2004).
- B. Li, J. Kung, T. Uchida, and Y. Wang, "Simultaneous equation of state, pressure calibration and sound velocity measurements to lower mantle pressures using multi-anvil apparatus," in *Advances in High-Pressure Technology for Geophysical Applications*, edited by J. Chen, Y. Wang, T. S. Duffy, G. Shen, and L. F. Dobrzynetska (Elsevier, New York, 2005).
- M. K. Jacobsen and N. Velisavljevic, "High pressure elasticity and thermal properties of depleted uranium," *J. Appl. Phys.* **119**, 165904 (2016).
- D. K. Mak, "Couplant correction for ultrasonic velocity-measurements," *British J. Non-Destruct. Test.* **33**, 344–346 (1991).
- D. K. Mak, "Ultrasonic phase-velocity measurement incorporating couplant correction," *British J. Non-Destruct. Test.* **35**, 443–449 (1993).
- C. Pantea, D. G. Rickel, A. Migliori, R. G. Leisure, J. Z. Zhang, Y. S. Zhao *et al.*, "Digital ultrasonic pulse-echo overlap system and algorithm for unambiguous determination of pulse transit time," *Rev. Sci. Instrum.* **76**, 114902 (2005).
- B. T. Sturtevant, C. Pantea, and D. N. Sinha, "Evaluation of the transmission line model for couplant layer corrections in pulse-echo measurements," *IEEE Trans. Ultrason., Ferroelectr. Freq. Control* **60**, 943–953 (2013).
- B. S. Li, K. Chen, J. Kung, R. C. Liebermann, and D. J. Weidner, "Sound velocity measurement using transfer function method," *J. Phys.: Condens. Matter* **14**, 11337–11342 (2002).
- Y. Kono, C. Park, T. Sakamaki, C. Kenny-Benson, G. Y. Shen, and Y. B. Wang, "Simultaneous structure and elastic wave velocity measurement of SiO₂ glass at high pressures and high temperatures in a Paris-Edinburgh cell," *Rev. Sci. Instrum.* **83**, 033905 (2012).
- B. A. Auld, *Acoustic Fields and Waves in Solids* (R.E. Krieger, 1990).
- Y. Kono, T. Irifune, Y. Higo, T. Inoue, and A. Barnhoorn, "P–V–T relation of MgO derived by simultaneous elastic wave velocity and *in situ* X-ray measurements: A new pressure scale for the mantle transition region," *Phys. Earth Planet. Inter.* **183**, 196–211 (2010).
- W. H. Press, S. A. Teukolsky, W. T. Vetterling, and B. P. Flannery, *Numerical Recipes in C*, 2nd ed. (Cambridge University Press, 1992).